Available online at www.sciencedirect.com
ScienceDirect
ELSEVIER
Journal of Sound and Vibration 309 (2008) 276–292
JOURNAL OF SOUND AND VIBRATION
www.elsevier.com/locate/jsvi

Nonlinear model and system identification of a capacitive dual-backplate MEMS microphone

Jian Liu[a,1], David T. Martin[b], Karthik Kadirvel[b], Toshikazu Nishida[b], Louis Cattafesta[a], Mark Sheplak[a], Brian P. Mann[c,*]

[a]Department of Mechanical and Aerospace Engineering, University of Florida, Gainesville, FL 32611-6250, USA
[b]Department of Electrical and Computer Engineering, University of Florida, Gainesville, FL 32611-6250, USA
[c]Department of Mechanical Engineering and Materials Science, Duke University, Durham, NC 27708, USA

Received 6 January 2006; received in revised form 29 November 2006; accepted 18 July 2007
Available online 14 September 2007

Abstract

This paper presents the nonlinear identification of a capacitive dual-backplate microelectromechanical systems (MEMS) microphone. First, a nonlinear lumped element model of the coupled electromechanical microphone dynamics is developed. Nonlinear finite element analyses are performed to verify the accuracy of the lumped linear and cubic stiffnesses of the diaphragm. In order to experimentally extract the system parameters, an approximate solution using the second-order multiple scales method is synthesized for a nonlinear microphone model, subject to an electrical step input. A nonlinear least-squares technique is then implemented to extract system parameters from laser vibrometry data of the diaphragm motion. The results indicate that the theoretical fundamental resonant frequency, damping ratio and nonlinear stiffness parameter agree with the corresponding extracted experimental parameters with 95% confidence interval estimates.
© 2007 Elsevier Ltd. All rights reserved.

1. Introduction

A microphone is a transducer that converts unsteady pressure inputs into an electrical signal and is widely employed in many applications such as sound field measurements [1], hearing aids [2], and acoustic arrays [3]. A variety of transduction schemes, such as piezoelectric, piezoresistive, capacitive, electrodynamic and optical, have been used in microphones [4,5]. The vast majority of microphones are based on the measurement of a pressure-induced structural deflection of a diaphragm.

The realization of low-cost, miniature instrumentation grade microphones is important for the development of aeroacoustic directional arrays used for noise source localization and characterization [3,6]. Traditional microphones, such as the Brüel & Kjær condenser microphones, offer excellent performance, but are costly and currently not suitable for miniaturization. With the development of microelectromechanical systems

*Corresponding author. Tel.: +1 919 660 5328; fax: +1 919 660 8963.
E-mail address: brian.mann@duke.edu (B.P. Mann).
[1]Now with AdaptivEnergy, LLC(formerly PAR Technologies, Inc.), Hampton, VA 23666, USA.

0022-460X/$ - see front matter © 2007 Elsevier Ltd. All rights reserved.
doi:10.1016/j.jsv.2007.07.037

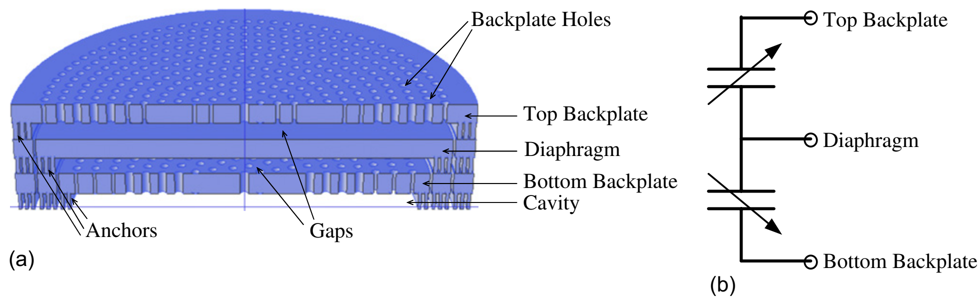

Fig. 1. Microphone structure and basic sensing mechanism. The graphs show (a) a 3D cross-section view of microphone structure (not to scale) and (b) a schematic of the electrical model of the microphone.

(MEMS) technology, hundreds or thousands of devices can be fabricated together on a single silicon wafer. This provides the opportunity to produce MEMS microphones that can approach the performance of traditional microphones with lower cost and smaller size [7].

One of the key performance metrics of an aeroacoustic microphone is the bandwidth, which should at least range from 45 Hz to 90 kHz to accommodate 1/8th-scale testing [6]. During the past decade, many research teams have developed or demonstrated capacitive MEMS microphones targeted at audio applications [2,8–14]. Audio applications, however, require lower maximum sound pressure levels (<120 dB, ref. 20 μPa), and the bandwidths are limited to 20 kHz. The development of capacitive MEMS microphones for the aeroacoustic applications presents several challenges. First, scaling capacitive transduction schemes to the microscale requires that the backplate is located in very close proximity to the diaphragm [4]. This close spacing may result in unacceptably high viscous damping loses, thus limiting the bandwidth of the microphone. Also, pull-in instabilities can be a potential issue [4,15]. A dual-backplate structure, that possesses porous electrodes or backplates on either side of the diaphragm (Fig. 1(a)), may be able to mitigate these challenges. Specifically, dual-backplate capacitive microphones offer the potential of smaller size, higher sensitivity, larger dynamic range and broader bandwidth over single-backplate capacitive microphones [2,4]. The dual-backplate capacitive MEMS microphone studied here has been fabricated using the SUMMiT V process at Sandia National Laboratories as well as facilities at the University of Florida for post-processing [16]. The microphone has a fundamental resonant frequency of over 218 kHz [17]. The overall performance of this microphone is expected to be further improved via the implementation of a force feedback controller [18].

The development of such a controller requires an accurate nonlinear model for the microphone system. The microphone system must be designed such that it is not operated in regions of pull-in instabilities that typically result in device structural failure. In addition, the stable operating range of the microphone can be potentially expanded by leveraging the mechanical nonlinearity. Therefore, a thorough understanding of nonlinear dynamics of the microphone is vital.

The remainder of this paper is organized as follows. First, a nonlinear governing equation for the microphone is developed by lumped element modeling in Section 2. Nonlinear finite element analyses are performed to verify the accuracy of the lumped linear and cubic stiffnesses of the diaphragm in Section 3. Nonlinear equations to identify system parameters of the microphone from the experiments are provided in Section 4. An approximate solution for the nonlinear oscillations of the diaphragm via the method of multiple time scales is discussed in Section 5. Section 6 presents the detailed experimental study, and an uncertainty analysis is conducted in Section 7. Conclusions are provided in Section 8.

2. Microphone model

A cross-sectional view for the microphone of interest is shown in Fig. 1(a). It has a 2.25 μm thick circular solid diaphragm with a 230 μm radius and a 2 μm gap between each circular perforated backplate. The 5 μm radius holes in the backplates allow the incident acoustic pressure to act on the diaphragm. A cavity under the bottom backplate is formed via a deep reactive ion etch, and vented to the ambient pressure resulting in an ac

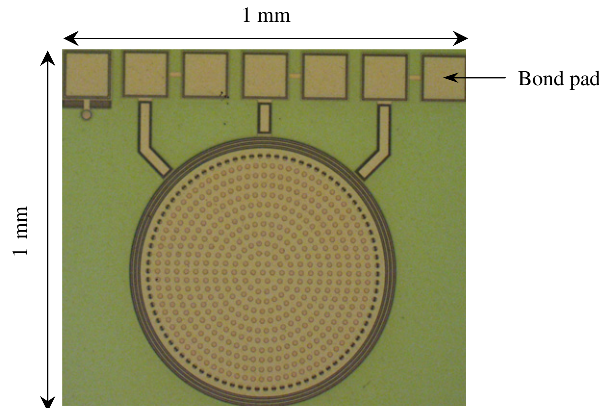

Fig. 2. Top-view optical photograph of the microphone.

measurement device. The three plates of the microphone are conductive; therefore, two capacitors exist between the diaphragm and each backplate as shown in Fig. 1(b). When an acoustic wave impinges on the microphone, the incident pressure deflects the middle diaphragm and thereby alters the capacitance of the two capacitors. The differential capacitance change is converted to an output voltage through various types of interface circuitry [19]. Fig. 2 shows a microscope photograph of the microphone top with a field of view of approximately 1 mm × 1 mm. The bond pads shown in the photograph enable electrical connections between the backplates and diaphragm.

2.1. Lumped element parameters

The microphone is a multiple energy domain (acoustical, mechanical and electrical) system governed by a set of coupled nonlinear partial differential equations. The analysis and design of coupled-domain transducer systems are commonly performed using lumped element models. The main assumption employed in lumped element modeling (LEM) is that the characteristic length scales of the governing physical phenomena are much larger than the largest geometric dimension. This quasi-static assumption limits the model validity up to frequencies beyond the fundamental natural frequency of the microphone [19,20]. This limitation does not adversely affect the design of microphone as the measurement bandwidth is usually defined to ± 3 dB of the flat band response which occurs near the first resonance [6].

The microphone diaphragm is treated as a linearly elastic, axisymmetric, clamped circular plate possessing no in-plane stress. From the theory of elasticity [21], the transverse displacement, $w(r)$, under a uniform pressure load is

$$w(r) = x\left[1 - \left(\frac{r}{a}\right)^2\right]^2, \tag{1}$$

where x is the center displacement of the diaphragm and will be defined later, r is the distance of any radial point along the radius, and a is the radius of the diaphragm.

The lumped element modeling of the diaphragm of the microphone is conducted via conjugate power variables in the mechanical energy domain, where force is the effort variable and velocity is the flow variable [19]. The diaphragm with distributed deflections is lumped into a rigid piston that translates with the center deflection of the diaphragm and possesses an equivalent mass, area and compliance.

The lumped mass is determined by equating the lumped kinetic energy at the center of the diaphragm to the total kinetic energy stored in the distributed deflections. In the mechanical domain, based on Eq. (1), the equivalent lumped mass, M_{me}, is calculated as [19,20]

$$M_{\mathrm{me}} = \tfrac{1}{5}\pi a^2 h\rho_d, \tag{2}$$

where h is the thickness of the diaphragm and ρ_d is the density of the diaphragm. Physically, in order to conserve the kinetic energy, a rigid piston with a mass that is 1/5 that of the actual diaphragm is used. Similarly, the effective area of the diaphragm, A_{me}, is determined by enforcing continuity of volume velocity [19,20],

$$A_{\mathrm{me}} = \tfrac{1}{3}\pi a^2. \tag{3}$$

The center displacement of the diaphragm, under a large transverse uniform pressure load, is given by the following expression when using an energy-based analytical approach [21]

$$x = \frac{pa^4}{64D}\frac{1}{1+0.4708x^2/h^2}, \tag{4}$$

where p is the applied acoustic pressure, and D is the flexural rigidity of the diaphragm defined as

$$D = \frac{Eh^3}{12(1-v^2)}, \tag{5}$$

where v and E are the Poisson's ratio and Young's modulus for the polysilicon diaphragm, respectively.

The factor $0.4708\,x^2/h^2$ in Eq. (4) represents a geometric nonlinearity due to the effect of in-plane stretching, which is significant and cannot be neglected when large displacements occur. If the center displacement is much smaller than the thickness of the diaphragm, it follows that Eq. (4) is reduced to its linear counterpart [21]. A more rigorous theory of the nonlinear mechanics of transducer diaphragms including the effects of in-plane stress is given in Ref. [22].

Eq. (4) indicates that the diaphragm behaves like a Duffing's hardening spring when large displacements occur. Based on the lumped element model, the Duffing's hardening spring model is written as

$$pA_{\mathrm{me}} = k_1 x + k_3 x^3, \tag{6}$$

where k_1 and k_3 are linear and cubic stiffnesses of the diaphragm, respectively. By comparing Eq. (6) with Eq. (4), k_1 and k_3 are obtained as

$$k_1 = \frac{64D\pi}{3a^2} \tag{7}$$

and

$$k_3 = \frac{10.044\,D\pi}{a^2h^2}. \tag{8}$$

The shallow cavity of the microphone impedes the motion of the diaphragm by storing potential energy, analogous to a spring. This process is considered isentropic since the adiabatic and inviscid assumptions are valid for the microphone operating frequency range. Based on the lumped element assumption, the equivalent mechanical stiffness, k_c, is calculated as follows [19,20,23]:

$$k_c = \frac{\rho_a c_0^2}{\pi a_c^2 d_c}(\pi a_c^2)^2 = \frac{\pi\rho_a c_0^2 a_c^2}{d_c}, \tag{9}$$

where c_0 is the isentropic speed of sound in air, ρ_a is the density of air, a_c and d_c are the radius and depth of the cavity cylinder, respectively. $(\pi a_c^2)^2$ is used to convert the acoustical stiffness into the mechanical stiffness.

When the diaphragm vibrates, the gas flow between the diaphragm and backplate is divided into two parts; the horizontal gas flow between the two parallel plates and the vertical gas flow through the circular backplate holes. Viscous damping caused by the horizontal gas flow in the gaps is often referred to as squeeze-film damping, its lumped damping coefficient, b^s, is given by [24,25]

$$b^s = \frac{4\mu\pi a^4}{3n_{\mathrm{bp}}d_0^3}f(A_{\mathrm{bp}}) + \frac{4\mu\pi a^4}{3n_{\mathrm{tp}}d_0^3}f(A_{\mathrm{tp}}), \tag{10}$$

where μ is the dynamic viscosity of air, d_0 is the nominal gap between backplates and diaphragm, n_{tp} and n_{bp} are total number of holes in the top and bottom backplates, respectively. The porosity of the top and bottom

backplates is given by A_{tp} and A_{bp}, respectively, and $f(\ )$ is a function with the following form:

$$f(X) = \frac{1}{4}\ln\left(\frac{1}{X}\right) - \frac{3}{8} + \frac{1}{2}X - \frac{1}{8}X^2. \tag{11}$$

When the thickness of the backplate is comparable to the gap, the viscous damping due to the vertical gas flow through the backplate holes becomes important. By modeling the motion in the holes as a pressure-driven Poiseuille flow in a pipe, the lumped damping coefficient, b^h, is given by [25]

$$b^h = \frac{8\,\mu\pi h_{\text{tp}} n_{\text{tp}}}{A_{\text{tp}}^2} + \frac{8\,\mu\pi h_{\text{bp}} n_{\text{bp}}}{A_{\text{bp}}^2}, \tag{12}$$

where h_{tp} and h_{bp} are the thicknesses of the top and bottom backplates, respectively. Therefore, the total lumped viscous damping, b, is given by

$$b = b^s + b^h. \tag{13}$$

2.2. Nonlinear dynamic model

Once all the lumped parameters are obtained, the microphone is represented by a single-degree-of-freedom second-order nonlinear ordinary differential equation with simplified dynamics appropriate for theoretical study. Fig. 3 shows a schematic of the dynamic model of the microphone. The top and bottom backplates are assumed to be rigid and have equal areas as the diaphragm. In general, if the top and bottom backplates are biased with respect to the middle diaphragm by two electrical signals ($\pm V(t)$) with equal magnitudes and opposite polarity, the dynamic equation of motion is [26]

$$\begin{aligned} &M_{\text{me}}\ddot{x} + b\dot{x} + (k_1 + k_c)x + k_3 x^3 \\ &= -\frac{\varepsilon_0 A_{\text{me}}}{2}\left[\frac{V(t)^2}{(d_0 + x)^2} - \frac{V(t)^2}{(d_0 - x)^2}\right] - pA_{\text{me}}, \end{aligned} \tag{14}$$

where an upward motion of the diaphragm is assumed to be positive, and a parallel-plate assumption is used when determining the electrostatic forces. Eq. (14) represents a nonlinear dynamic system with coupled cubic

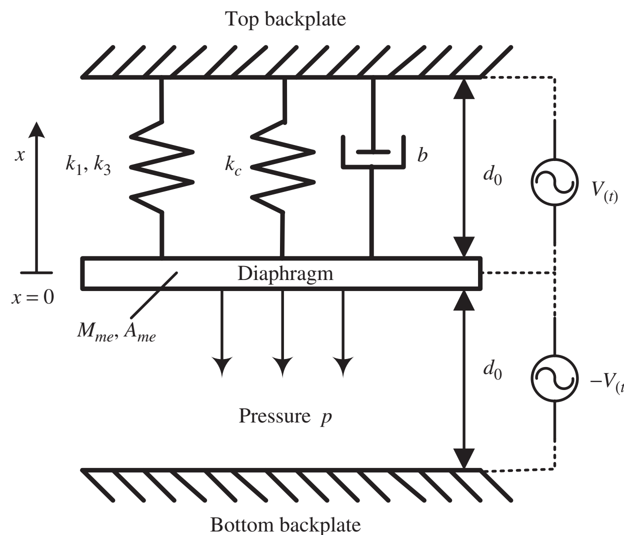

Fig. 3. Nonlinear dynamic model of a dual-backplate MEMS microphone.

Table 1
Physical dimensions, material properties [31] and theoretical lumped parameters of the microphone

Property	Nominal value	Lumped parameter	Nominal value
a	230.0 μm	k_1	202.2 N/m
a_c	187.0 μm	k_3	1.880×10^{13} N/m^3
d_0	2.000 μm	k_c	24.27 N/m
d_c	650.0 μm	M_{me}	1.668×10^{-10} kg
h	2.250 μm	A_{me}	5.540×10^{-8} m^2
h_{tp}	2.250 μm	b	3.145×10^{-5} N s/m
h_{bp}	2.500 μm	ξ	8.091×10^{-2}
E	160.0 GPa	$\omega_0/2\pi$	185.5 kHz
ρ	2.230×10^3 kg/m^3	β	1.127×10^{23} N/m^3/kg
v	0.220	Γ	332.2 m^2/kg

mechanical and electrostatic nonlinearities,

$$\ddot{x} + 2\,\xi\omega_0\dot{x} + \omega_0^2 x + \beta x^3 = -\frac{\varepsilon_0\Gamma}{2}\left[\frac{V(t)^2}{(d_0+x)^2} - \frac{V(t)^2}{(d_0-x)^2}\right] - p\Gamma, \tag{15}$$

where $\omega_0 = \sqrt{(k_1+k_c)/M_{me}}$ is the fundamental resonant frequency, $\xi = b/(2M_{me}\omega_0)$ is the damping ratio, $\beta = k_3/M_{me}$ is the nonlinear stiffness parameter and $\Gamma = A_{me}/M_{me}$ is the ratio of lumped area over lumped mass.

A list of the primary physical dimensions and material properties is given in Table 1. The theoretical lumped element model parameters that correspond to these dimensions and material properties are also listed in Table 1.

3. Nonlinear FEA verification

This section describes the steps taken to verify the accuracy of the theoretical lumped element stiffnesses, namely k_1 and k_3 of the diaphragm model. Three-dimensional (3D) nonlinear finite element analyses (FEA) are carried out using a commercial software package, CoventorWare by Coventor, Inc.,[2] to extract the lumped mechanical stiffnesses of the diaphragm. The 3D mesh of the diaphragm has 82452 solid brick elements and the average aspect ratio of the mesh is approximately 1.62. Based on this mesh, converged displacement results have been achieved with the diaphragm under the applied uniform pressure.

The material properties and physical dimensions of the diaphragm used in the FEA are taken from Table 1. The side surface of the diaphragm is clamped for the boundary condition. A series of uniform pressures with amplitudes varying from 10 to 4000 Pa are applied to the top surface of the diaphragm and the FEA are carried out to yield the transverse center deflection of the diaphragm for each applied pressure.

Fig. 4 shows a plot of transverse center deflections of the diaphragm. The ideal linear, energy-based analytical as well as exact analytical deflection results (from Ref. [22]) are also plotted in Fig. 4. As seen from the plot, three sets of nonlinear deflection results are in good agreement with each other. The mechanical nonlinearity becomes important for the large applied pressure, for example, when the pressure value is above 2000 Pa.

The lumped linear and cubic stiffnesses are extracted by curve-fitting the simulated nonlinear center displacements of the diaphragm with the formula in Eq. (6), and the final results are listed in Table 2. From the table, the differences between the theoretical and FEA linear and cubic stiffnesses are approximately 1.3% and 5.0%, respectively.

[2]Commercial software is identified for completeness and does not imply endorsement by the authors.

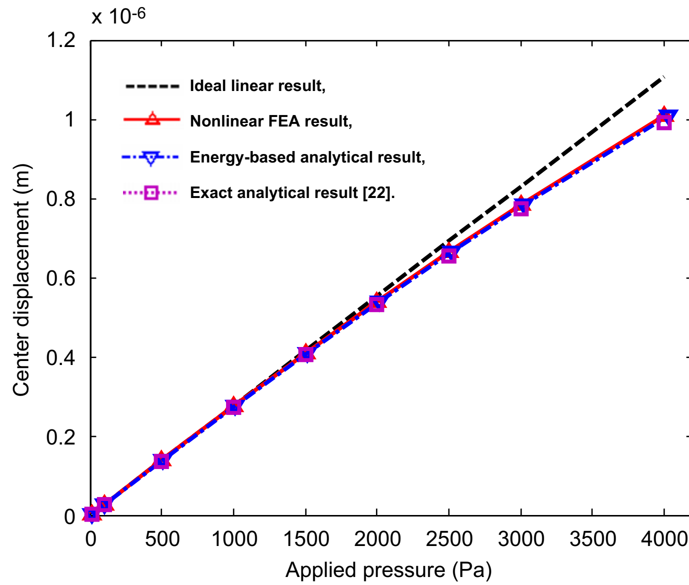

Fig. 4. Transverse center deflections of the diaphragm under the uniform pressure. -----, ideal linear result; —△—, nonlinear FEA result; -▽-, energy-based analytical result; ···□···, exact analytical result [22].

Table 2
Comparison of nonlinear FEA and LEM results

Result	Linear stiffness k_1 (N/m)	Cubic stiffness k_3 (N/m^3)
Nonlinear FEA	199.7	1.979×10^{13}
LEM	202.2	1.880×10^{13}
Difference	1.252%	5.003%

4. Nonlinear equations for experiments

As seen from Eq. (15), system parameters (ξ, ω_0, β, and Γ) determine the dynamic behavior of the microphone. Although system parameters can be calculated theoretically from LEM, it is well-known that some of the modeling assumptions are idealizations. For example, the actual device possesses a finite amount of compliance in the diaphragm boundary conditions. Also the backplates are compliant and have slightly different areas. Therefore, some errors will exist between the theoretical and actual system parameters, and characterization experiments are required to determine the actual system parameters to evaluate the accuracy of the theoretical model.

Because the capacitive microphone is a reciprocal electromechanical transducer, the dynamics of the device can be deduced by measuring the diaphragm motion when driven by electrostatic forcing in a quiescent acoustic field. In this study, a unipolar square wave with a duty cycle of 0.5, $V(t)$, was applied directly to either the top or bottom backplate with the diaphragm and the other backplate both electrically grounded. The expression for the applied unipolar square pulse is

$$V(t) = \begin{cases} V_0, & nT \leqslant t < nT + \frac{T}{2}, \\ 0, & nT + \frac{T}{2} \leqslant t < (n+1)T, \end{cases} \tag{16}$$

where V_0 and T are the voltage amplitude and period of the square pulse, respectively, and $n = 0,1,2,\ldots$.

During the time $nT+T/2 \leqslant t < (n+1)$, no electrostatic force acts on the diaphragm, the governing equation for the free vibration of diaphragm is

$$\ddot{x} + 2\xi\omega_0\dot{x} + \omega_0^2 x + \beta x^3 = 0. \tag{17}$$

During the time $nT \leqslant t < nT+T/2$, an electrostatic force acts on the diaphragm and forces it to vibrate. The backplates are assumed to be symmetric about the diaphragm. Therefore, only the governing equation for the case in which the square pulse is applied to the top backplate is considered in the following analysis:

$$\ddot{x} + 2\xi\omega_0\dot{x} + \omega_0^2 x + \beta x^3 = \frac{\varepsilon_0\Gamma}{2}\frac{V_0^2}{(d_0 - x)^2}. \tag{18}$$

The above electrostatic force has a singularity at $x = d_0$. For $|x| < d_0$, a Taylor's series expansion for the nonlinear electrostatic force, about $x = 0$ and up to the third order, results in a convenient polynomial expression:

$$\frac{\varepsilon_0\Gamma}{2}\frac{V_0^2}{(d_0 - x)^2} \approx \frac{\varepsilon_0\Gamma V_0^2}{2d_0^2}\left[1 + 2\frac{x}{d_0} + 3\left(\frac{x}{d_0}\right)^2 + 4\left(\frac{x}{d_0}\right)^3\right]. \tag{19}$$

As seen from Eq. (19), a spring softening effect is introduced by the nonlinear electrostatic force. It follows that Eq. (18) is written as

$$\ddot{x} + \alpha_1\dot{x} + \alpha_2 x + \alpha_3 x^2 + \alpha_4 x^3 = \alpha_5, \tag{20}$$

where

$$\alpha_1 = 2\xi\omega_0, \tag{21}$$

$$\alpha_2 = \omega_0^2 - \frac{\varepsilon_0\Gamma V_0^2}{d_0^3}, \tag{22}$$

$$\alpha_3 = -\frac{3\varepsilon_0\Gamma V_0^2}{2d_0^4}, \tag{23}$$

$$\alpha_4 = \beta - \frac{2\varepsilon_0\Gamma V_0^2}{d_0^5}, \tag{24}$$

and

$$\alpha_5 = \frac{\varepsilon_0\Gamma V_0^2}{2d_0^2}. \tag{25}$$

Eq. (20) represents a general damped second-order system with both quadratic and cubic nonlinearities and a non-zero external step load, and its approximate analytical solution is obtained in the following section.

5. Approximate solution by multiple time scales

Since there is no closed form solution to Eq. (20), a multiple time scales approach [26,27] is used to obtain the approximate solution. The approximate solution of Eq. (20) is assumed as a second-order expansion in terms of a small positive parameter ε, which is a measure of the amplitude of the motion,

$$x(\tau_0, \tau_1, \tau_2, \varepsilon) = x_0(\tau_0, \tau_1, \tau_2) + \varepsilon x_1(\tau_0, \tau_1, \tau_2) + \varepsilon^2 x_2(\tau_0, \tau_1, \tau_2), \tag{26}$$

where x_0, x_1, and x_2 are three unknown functions, and the multiple independent time scales are defined as

$$\tau_0 = t, \quad \tau_1 = \varepsilon t \text{ and } \tau_2 = \varepsilon^2 t. \tag{27}$$

The coefficients in Eq. (20) are further ordered to show up in the $O(\varepsilon^2)$ by performing the following substitution:

$$\alpha_1 = \varepsilon^2\mu_1,\ \alpha_2 = \omega^2,\ \alpha_3 = \varepsilon^2\mu_3 \text{ and } \alpha_4 = \varepsilon^2\mu_4. \tag{28}$$

Eqs. (26)–(28) are then substituted into Eq. (20) and the coefficients of the $O(\varepsilon)$ are collected to arrive a series of equations. The result of the solution process, which is detailed in Appendix A, gives the following approximate solution to Eq. (20):

$$x(t) = \frac{\alpha_5}{\alpha_2} + R_0 \mathrm{e}^{-1/2\alpha_1 t} \cos\left[\left(\omega + \frac{2\alpha_2\alpha_3\alpha_5 + 3\alpha_4\alpha_5^2}{2\omega\alpha_2^2}\right)t - \frac{3\alpha_4 R_0^2}{8\omega\alpha_1}\mathrm{e}^{-\alpha_1 t} + \phi_0\right]. \tag{29}$$

If an initial displacement χ_0 is imposed and the system starts from rest, the resulting transient displacement becomes

$$x(t) = \frac{\alpha_5}{\alpha_2} + \widehat{\chi}_0 \mathrm{e}^{-1/2\alpha_1 t} \cos\left[\left(\omega + \frac{2\alpha_2\alpha_3\alpha_5 + 3\alpha_4\alpha_5^2}{2\omega\alpha_2^2}\right)t - \frac{3\alpha_4 \widehat{\chi}_0^2}{8\omega\alpha_1}(\mathrm{e}^{-\alpha_1 t} - 1)\right], \tag{30}$$

where

$$\widehat{\chi}_0 = \chi_0 - \frac{\alpha_5}{\alpha_2}. \tag{31}$$

If there is no external step loading and quadratic nonlinearity in the system ($\alpha_3 = 0$ and $\alpha_5 = 0$), which occurs for the experimental case of transients about a zero equilibrium position, Eq. (30) is then reduced into

$$x(t) = \chi_0 \mathrm{e}^{-1/2\alpha_1 t} \cos\left[\omega t - \frac{3\alpha_4\chi_0^2}{8\omega\alpha_1}(\mathrm{e}^{-\alpha_1 t} - 1)\right]. \tag{32}$$

Eq. (32) is easily applied to Eq. (17) to yield the following solution:

$$x(t) = \chi_0 \mathrm{e}^{-\xi\omega t} \cos\left[\omega t - \frac{3\beta\chi_0^2}{16\xi\omega^2}(\mathrm{e}^{-2\xi\omega t} - 1)\right]. \tag{33}$$

Once α_1, α_2, α_3, α_4, and α_5 are estimated by a nonlinear least-squares curve-fitting technique based on the time history of experimental transient displacement, system parameters ξ, ω_0, β, Γ, and d_0 are then identified by solving Eqs. (21)–(25) simultaneously as follows:

$$d_0 = \sqrt{-3\frac{\alpha_5}{\alpha_3}}, \tag{34}$$

$$\Gamma = \frac{2d_0^2\alpha_5}{\varepsilon_0 V_0^2}, \tag{35}$$

$$\omega_0 = \sqrt{\alpha_2 + \frac{\varepsilon_0 V_0^2 \Gamma}{d_0^3}}, \tag{36}$$

$$\xi = \frac{\alpha_1}{2\omega_0} \tag{37}$$

and

$$\beta = \alpha_4 + \frac{2\varepsilon_0 V_0^2 \Gamma}{d_0^5}. \tag{38}$$

6. Experimental study

The characterization experiment of the microphone was conducted using the scanning laser Doppler vibrometer (Polytec MSV 300). The block diagram of the experiment setup is shown in Fig. 5 and is discussed further below.

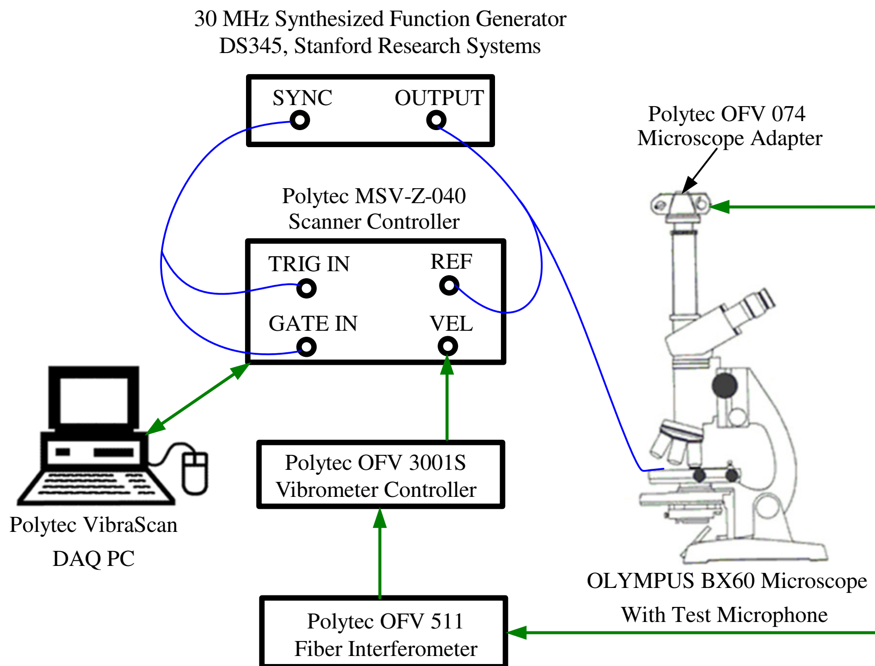

Fig. 5. Block diagram of the experimental setup.

6.1. Experiment setup

The test microphone is positioned on the stage of a microscope (OLYMPUS BX60). A fiber interferometer (OFV 511) generates the input laser beam and receives the resulting interference optical signal through a microscope adapter (OFV 074). The resulting optical signal is converted into an electrical signal by the photodetector inside the fiber interferometer and subsequently decoded by a vibrometer controller (OFV 3001S) to generate the velocity. The velocity output from the Vibrometer controller is then connected to the "VEL" channel of a scanner controller (MSV-Z-040). A data acquisition PC (VibraScan) acquires data from both "REF" and "VEL" channels in the scanner controller [28]. The output of the function generator (DS345, Stanford Research Systems) is used to provide the electrical signal to electromechanically excite the microphone under the microscope. It should be pointed out that two function generators in series with phase locked are used to output the high voltage signal (>10 V) in the experiments.

Fig. 6 shows an optical photograph of a laser beam spot, which was positioned inside the center hole of the top backplate so that the center velocity response of the diaphragm was measured during the experiments. A sampling rate of 2.56 MHz was used to record the velocity for 3.2 ms; 100 ensemble averages were used to minimize the noise in the measured velocity data.

As mentioned previously, during the high part (up-stroke) of the square pulse cycle, the vibration of the diaphragm is forced by the external electrostatic force, and free response occurs during the low part (down-stroke) of the square pulse cycle. In order to let the transient free response of the diaphragm decay completely before the follow-up forced response, a 1 kHz repetition frequency is used.

When the characterization experiments using the top backplate for actuation is conducted, the middle diaphragm and the bottom backplate are electrically grounded. The square pulse was then applied directly to the top backplate of the microphone, and the dynamic response of the center velocity of the diaphragm was recorded for 100 ensembles. The above process was repeated several times for square pulses with different voltage amplitudes. Similarly, the characterization experiments using the bottom backplate for actuation are conducted with the middle diaphragm and the top backplate electrically grounded.

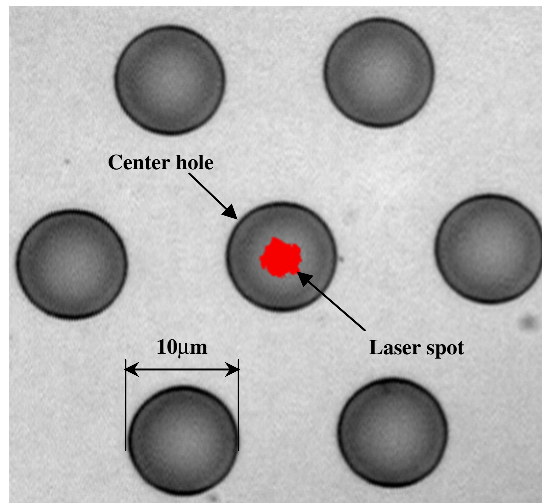

Fig. 6. An optical photograph showing a laser beam spot impinges on the diaphragm through the center hole of the top backplate.

6.2. Results

The trapezoidal rule is applied to numerically integrate the measured average center velocity to yield the center displacement [29]. Because the time step is very small (0.39 μs), the numerical integration error is minute and was assumed to be negligible. Also, a measurement velocity resolution of 1.5 μm/s is used in this study [28]; therefore, the calculated minimum detectable displacement is approximately 2.4 pm at 100 kHz and 0.24 pm at 1 MHz.

The experimental tests for the top backplate are discussed first with results shown in Fig. 7. Fig. 7(a) shows the measured ensemble-averaged center velocity response (i.e. the up-stroke) of the diaphragm. As seen from the plot, the center velocity decays quickly to zero. The corresponding integrated center displacement response is shown in Fig. 7(b). Based on the measured velocity and integrated displacement response, a constructed phase plot after 12 μs is generated in Fig. 7(c), showing the system spirals into a fixed point.

By using Eq. (30), a nonlinear least-squares curve-fitting procedure is carried out in MATLAB to obtain system parameters ξ, ω_0, β, Γ, and d_0 from the transient response data of the integrated center displacement. Shown in Fig. 7(d) is the comparison plot of the integrated and curve-fit center displacement results. The nonlinear least-squares curve-fit results are in good agreement with the integrated results. The curve-fit system parameter results are summarized in Table 3.

A similar set of experiments is performed using the bottom backplate and the results are shown in Fig. 8. The drift in the steady state of the integrated center displacement response in Fig. 8(b) is due to the experiment setup because the laser vibrometer does not measure the static displacement. It should be pointed out that the system parameters are extracted only from the transient response data of the integrated center displacement. Therefore, the accuracy of the extracted system parameters is not affected by the undesired drift. Similarly, a nonlinear least-squares curve-fitting procedure is carried out and the curve-fit system parameter results are summarized in Table 3.

7. Uncertainty analysis and discussion

In the previous sections, no uncertainties were assumed in the physical dimensions and/or material properties of the microphone. However, there always exists some uncertainty sources [30] in the real microphone device and experiments. For example, variations in physical dimensions and material properties, which are caused by the fabrication process, can often substantially alter the model parameters of a MEMS device.

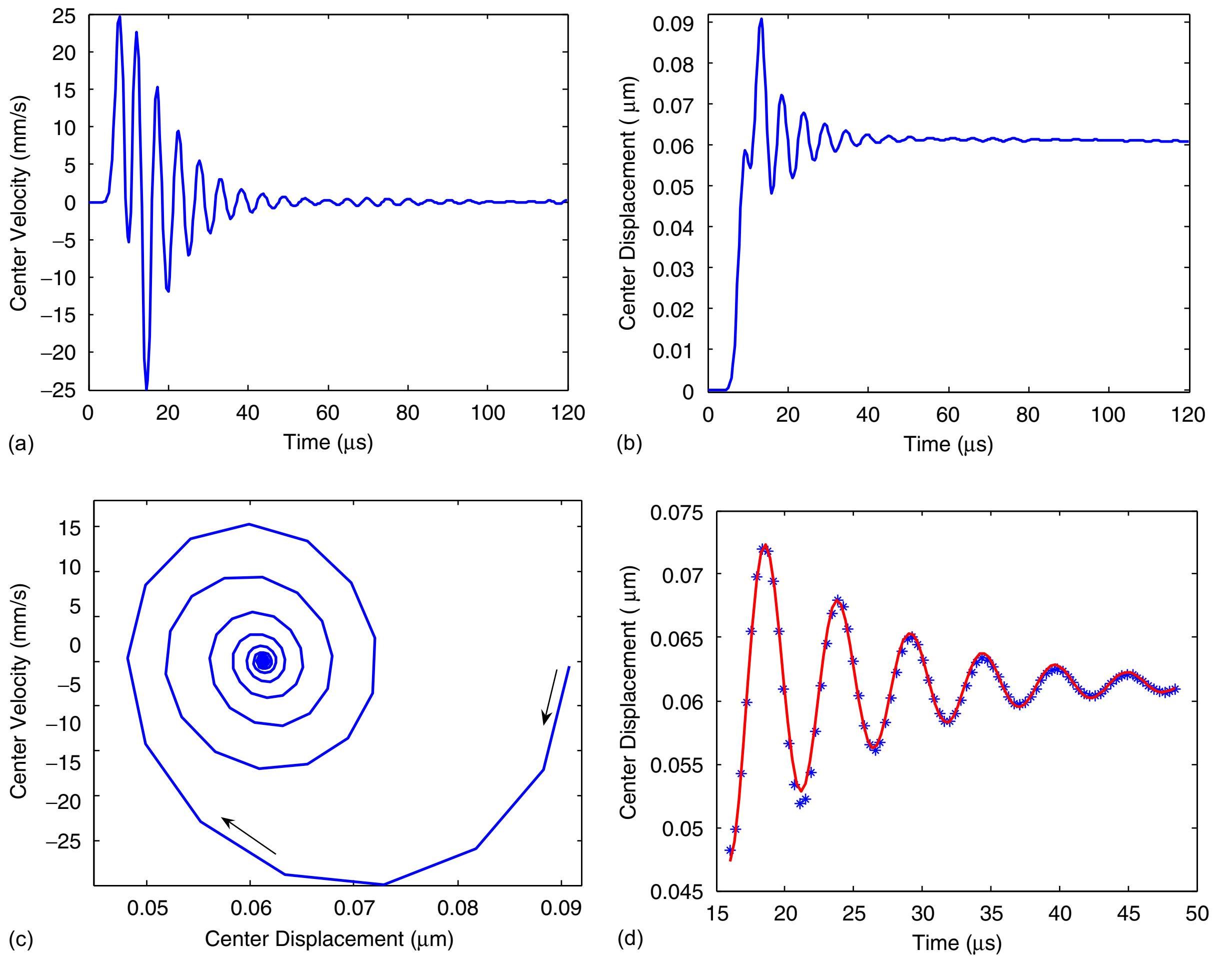

Fig. 7. Results for the top backplate excitation by a unipolar 1 kHz square wave with an amplitude of 18 V. The graphs show: (a) the measured average center velocity, (b) the integrated center displacement, (c) a constructed phase plot after 12 µs, and (d) a comparison of integrated (asterisk markers) and curve-fit (solid line) center displacements.

Table 3
Nonlinear least-squares curve-fit results for both the top and bottom backplate excitations

System parameter	Top backplate excitation result	Bottom backplate excitation result
ξ	7.791×10^{-2}	6.970×10^{-2}
d_0	1.950 µm	2.052 µm
$\omega_0/2\pi$	196.0 kHz	188.0 kHz
β	1.079×10^{23} N/m^3/kg	1.224×10^{23} N/m^3/kg
Γ	231.9 m^2/kg[a]	112.6 m^2/kg[b]

[a]Value for 18 V.
[b]Value for 5 V.

To carry out the uncertainty analysis, three uncertainty sources are considered: the uncertainty from the measured velocity and integrated displacement; the uncertainty associated with the approximate solution and nonlinear least-squares algorithm; and the uncertainty induced by the fabrication process. Further numerical simulations show that the limits of the approximate solution are sufficient for the experiments. Also, further

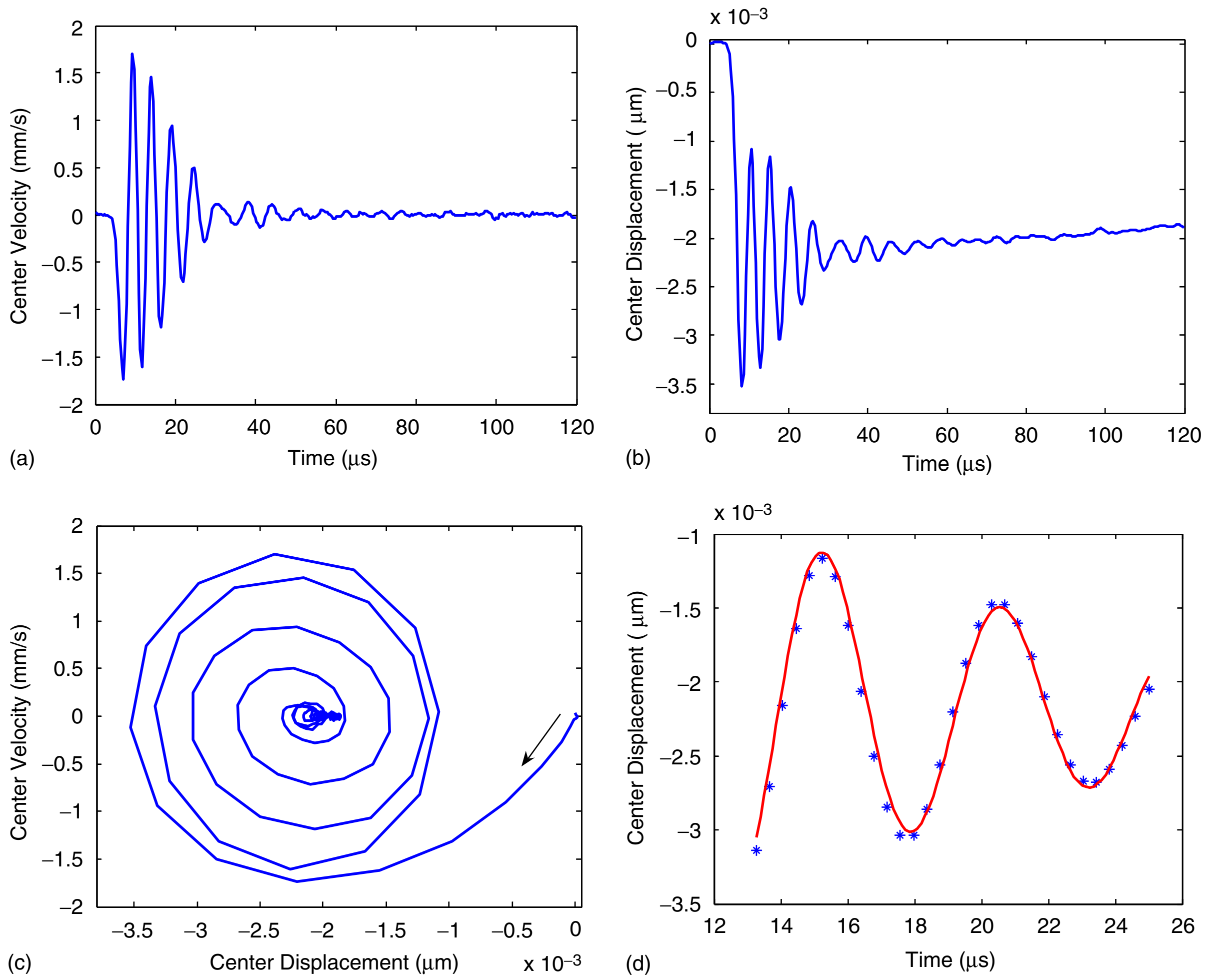

Fig. 8. Results for the bottom backplate excitation by a unipolar 1 kHz square wave with an amplitude of 5 V. The graphs show: (a) the measured average center velocity, (b) the integrated center displacement, (c) a constructed phase plot, and (d) a comparison of integrated (asterisk markers) and curve-fit (solid line) center displacements.

study shows that the fabrication-induced parameter uncertainties are large and dominant compared to other uncertainties, thereafter only the uncertainties caused by the fabrication process are considered in the following analysis.

From the reproducibility datasheet of the fabrication [31], for the 95% confidence interval, the thickness of the diaphragm is $2.27 \pm 0.02\,\mu m$. The thickness of the top backplate is $2.27 \pm 0.012\,\mu m$. The thickness of the bottom backplate is $2.51 \pm 0.006\,\mu m$. The gap between diaphragm and bottom backplate is $2.2 \pm 0.5\,\mu m$, and the gap between diaphragm and top backplate is $2.0 \pm 0.5\,\mu m$. For the Young's modulus of polysilicon, 173 ± 20 GPa is used [32]. These uncertainties are propagated into the calculated system parameters using standard methods [33]. The final uncertainty analysis results are summarized in Table 4. As seen from Tables 1 and 4, the nominal values of system parameters ξ, ω_0, β, and Γ fall into their uncertainty estimates.

From Tables 1 and 4, the theoretical fundamental resonant frequency, damping ratio and nonlinear stiffness parameter agree with the corresponding extracted experimental parameters with 95% confidence interval estimates. Also, small differences exist between the experimentally identified system parameters for both bottom and top single backplate microphones, respectively. The discrepancies are mainly due to the different bottom and top capacitors, such as unequal air gaps and electrode areas.

Table 4
Mean values and uncertainties of system parameters for a given 95% confidence level

System parameter	Mean	Uncertainty
ξ	7.272×10^{-2}	1.337×10^{-2}
$\omega_0/2\pi$ (kHz)	193.5	10.20
β (N/m^3/kg)	1.219×10^{23}	0.1409×10^{23}
Γ (m^2/kg)	329.2	2.901

It is shown that Γ is a constant from the lumped element model based on a simple equal-area parallel plate assumption. However, experimental results of Γ indicate that it is a function of the applied voltage; which means that the equivalent area for calculating electrostatic forces depends on the applied voltage (assuming the lumped mass is fixed). The changing experimental behavior of Γ could be due to several reasons. In the actual physical device, the area of the top compliant backplate is larger than the area of the diaphragm, which is larger than the area of the bottom compliant backplate. Therefore, the equal-area assumption is not accurate in practice [34]. The overlapping area could change due to the different bending shapes of the plates when different voltages are applied between the perforated backplate and diaphragm.

8. Conclusions

This paper presents the development of a nonlinear model and the experimental characterization of a dual-backplate MEMS microphone that was fabricated for high-frequency aeroacoustic applications. LEM is used to estimate system parameters for a nonlinear dynamic model in which the microphone is governed by a second-order ordinary differential equation with electrostatic and cubic mechanical nonlinearities. Nonlinear finite element analyses show that the differences between the theoretical and FEA linear and cubic stiffnesses of the diaphragm are approximately 1.3% and 5.0%, respectively. The approximate solution to the nonlinear microphone model, subjected to a unipolar square wave, is explored by the second-order multiple time scales method. Based on the approximate solution, a nonlinear least-squares algorithm is implemented to extract system parameters from the experimental data. An uncertainty analysis shows that the theoretical fundamental resonant frequency, damping ratio and nonlinear stiffness parameter agree with the corresponding extracted experimental parameters with 95% confidence interval estimates. Experimental results of the ratio of lumped area over lumped mass (Γ) suggest that it is a function of the applied voltage, and the discrepancy between its theoretical and experimental values is likely due to the inaccurate assumption of equal-area parallel plates when the electrostatic force is calculated.

Acknowledgments

Financial support was provided by a National Science Foundation Grant (ECS-0097636), a CAREER Award (CMS-0636641), and Sandia National Laboratories.

Appendix A. Derivation of the approximate solution to Eq. (20)

The details for the approximate solution to Eq. (20) are provided in this appendix. Since the multiple independent time scales are defined in Eq. (27), the time derivatives with respect to t become the following expansion terms of the partial derivatives with respect to the corresponding time scales:

$$\frac{\mathrm{d}}{\mathrm{d}t} = D_0 + \varepsilon D_1 + \varepsilon^2 D_2 \tag{A.1}$$

and

$$\frac{\mathrm{d}^2}{\mathrm{d}t^2} = D_0^2 + 2\varepsilon D_0 D_1 + 2\varepsilon^2 D_0 D_2 + \varepsilon^2 D_1^2, \tag{A.2}$$

where

$$D_0=\frac{\mathrm{d}}{\mathrm{d}\tau_0}, D_1=\frac{\mathrm{d}}{\mathrm{d}\tau_1} \text{ and } D_2=\frac{\mathrm{d}}{\mathrm{d}\tau_2}. \tag{A.3}$$

Substitution of Eqs. (26)–(28), (A.1)–(A.3) into Eq. (20) results in the following expressions after separating into the $O(\varepsilon)$:

$$O(\varepsilon^0):\ D_0^2x_0+\omega^2x_0=\alpha_5, \tag{A.4}$$

$$O(\varepsilon^1):\ D_0^2x_1+\omega^2x_1=-2D_0D_1x_0 \tag{A.5}$$

and

$$O(\varepsilon^2):\ D_0^2x_2+\omega^2x_2=-2\,D_0D_1x_1-2\,D_0D_2x_0-D_1^2x_0-\mu_1D_0x_0-\mu_3x_0^2-\mu_4x_0^3. \tag{A.6}$$

The general solution to Eq. (A.4) is

$$x_0=\frac{\alpha_5}{\alpha_2}+A(\tau_1,\tau_2)\mathrm{e}^{\mathrm{i}\omega\tau_0}+\bar{A}(\tau_1,\tau_2)\mathrm{e}^{-\mathrm{i}\omega\tau_0}, \tag{A.7}$$

where $A(\tau_1,\tau_2)$ and $\bar{A}(\tau_1,\tau_2)$ are complex conjugates. The following expression is obtained by substituting Eq. (A.7) into Eq. (A.5):

$$D_0^2x_1+\omega^2x_1=-2\mathrm{i}\omega\left[\mathrm{e}^{\mathrm{i}\omega\tau_0}D_1A(\tau_1,\tau_2)-\mathrm{e}^{-\mathrm{i}\omega\tau_0}D_1\bar{A}(\tau_1,\tau_2)\right]. \tag{A.8}$$

The elimination of the secular terms from Eq. (A.8) requires that $D_1A(\tau_1,\tau_2)$ and $D_1\bar{A}(\tau_1,\tau_2)$ are zero, which means that A and $\bar{A}$ are only functions of τ_2.

Therefore, the solution for Eq. (A.8) is written as

$$x_1=B(\tau_1,\tau_2)\mathrm{e}^{\mathrm{i}\omega\tau_0}+\bar{B}(\tau_1,\tau_2)\mathrm{e}^{-\mathrm{i}\omega\tau_0}, \tag{A.9}$$

where $B(\tau_1,\tau_2)$ and $\bar{B}(\tau_1,\tau_2)$ are complex conjugates. Substituting Eqs. (A.7) and (A.9) into Eq. (A.6) yields

$$\begin{aligned}D_0^2x_2+\omega^2x_2=\Bigg[&-2\mathrm{i}\omega(D_1B)-2\mathrm{i}\omega(D_2A)-2\mu_3\frac{\alpha_5}{\alpha_2}A\\&-\mathrm{i}\mu_1\omega A-3\mu_4\left(\frac{\alpha_5^2}{\alpha_2^2}+|A|^2\right)A\Bigg]\mathrm{e}^{\mathrm{i}\omega\tau_0}+\text{O.H.T.},\end{aligned} \tag{A.10}$$

where O.H.T. are other harmonic terms that are neglected in the following analysis.

The elimination of the secular terms in Eq. (A.10) requires

$$-2\mathrm{i}\omega(D_1B)-2\mathrm{i}\omega(D_2A)-\mathrm{i}\mu_1\omega A-2\mu_3\frac{\alpha_5}{\alpha_2}A-3\mu_4\left(\frac{\alpha_5^2}{\alpha_2^2}+|A|^2\right)A=0. \tag{A.11}$$

It follows that B is only a function of τ_2 [27], therefore

$$-2\mathrm{i}\omega D_2A-\mathrm{i}\mu_1\omega A-\left(2\mu_3\frac{\alpha_5}{\alpha_2}+3\mu_4\frac{\alpha_5^2}{\alpha_2^2}\right)A-3\mu_4A|A|^2=0. \tag{A.12}$$

The polar form for the $A(\tau_2)$ is written as

$$A(\tau_2)=\tfrac{1}{2}R(\tau_2)\mathrm{e}^{\mathrm{i}\phi(\tau_2)}, \tag{A.13}$$

where R is the amplitude of x_0 and ϕ is the phase angle. Substituting Eq. (A.13) into (A.12) and separating into real and imaginary components results in

$$\frac{\mathrm{d}R}{\mathrm{d}\tau_2}+\frac{1}{2}\mu_1R=0 \tag{A.14}$$

and

$$\frac{\mathrm{d}\phi}{\mathrm{d}\tau_2}-\frac{2\mu_3\alpha_5\alpha_2+3\mu_4\alpha_5^2}{2\omega\alpha_2^2}-\frac{3\mu_4}{8\omega}R^2=0. \tag{A.15}$$

The solutions for R and ϕ are

$$R(\tau_2) = R_0 \mathrm{e}^{-1/2\mu_1\tau_2} \tag{A.16}$$

and

$$\phi(\tau_2) = \frac{2\,\mu_3\alpha_5\alpha_2 + 3\,\mu_4\alpha_5^2}{2\,\omega\alpha_2^2}\tau_2 - \frac{3\,\mu_4 R_0^2}{8\,\omega\mu_1}\,\mathrm{e}^{-\mu_1\tau_2} + \phi_0, \tag{A.17}$$

where R_0 and ϕ_0 are constants determined by initial conditions. Combining Eqs. (26), (A.7), (A.13), (A.16), and (A.17), the approximate solution is

$$x(\tau_0,\tau_1,\tau_2) \approx \frac{\alpha_5}{\alpha_2} + R_0\mathrm{e}^{-1/2\mu_1\tau_2}\cos\left(\omega\tau_0 + \frac{2\mu_3\alpha_5\alpha_2 + 3\mu_4\alpha_5^2}{2\omega\alpha_2^2}\tau_2 - \frac{3\mu_4R_0^2}{8\omega\mu_1}\mathrm{e}^{-\mu_1\tau_2} + \phi_0\right). \tag{A.18}$$

Using Eqs. (27) and (28), Eq. (A.18) is further simplified as

$$x(t) = \frac{\alpha_5}{\alpha_2} + R_0\mathrm{e}^{-1/2\alpha_1 t}\cos\left[\left(\omega + \frac{2\alpha_2\alpha_3\alpha_5 + 3\alpha_4\alpha_5^2}{2\omega\alpha_2^2}\right)t - \frac{3\alpha_4R_0^2}{8\omega\alpha_1}\mathrm{e}^{-\alpha_1 t} + \phi_0\right]. \tag{A.19}$$

References

[1] P.R. Scheeper, B. Nordstrand, J.O. Gullov, B. Liu, T. Clausen, L. Midjord, T. Storgaard-Larsen, A new measurement microphone based on MEMS technology, *Journal of Microelectromechanical Systems* 12 (2003) 880–891.

[2] J. Bay, O. Hansen, S. Bouwstra, Design of a silicon microphone with differential read-out of a sealed double parallel-plate capacitor, *Sensors and Actuators A* 53 (1996) 232–236.

[3] D.P. Arnold, T. Nishida, L.N. Cattafesta, M. Sheplak, A directional acoustic array using silicon micromachined piezoresistive microphones, *Journal of the Acoustical Society of America* 113 (1) (2003) 289–298.

[4] P.R. Scheeper, A.G.H. van der Donk, W. Olthuis, P. Bergveld, A review of silicon microphones, *Sensors and Actuators A* 44 (1994) 1–11.

[5] N.A. Hall, B. Bicen, M.K. Jeelani, W. Lee, S. Qureshi, F.L. Degertekin, Micromachined microphone with diffraction-based optical displacement detection, *Journal of the Acoustical Society of America* 118 (5) (2005) 3000–3009.

[6] T.J. Mueller, *Aeroacoustic Measurements*, Springer, Berlin, Heidelberg, 2002.

[7] S. Bouwstra, T. Storgaard-Larsen, P.R. Scheeper, J.O. Gullov, J. Bay, M. Mullenborg, P. Rombach, Silicon microphones—a Danish perspective, *Journal of Micromechanics and Microengineering* 8 (1998) 64–68.

[8] T. Bourouina, S. Spirkovitch, F. Baillieu, C. Vauge, A new silicon condenser microphone with a p^+ silicon membrane, *Sensors and Actuators A* 31 (1992) 149–152.

[9] Q. Zou, Z. Liu, L. Liu, Theoretical and experimental studies of single-chip-processed miniature silicon condenser microphone with corrugated diaphragm, *Sensors and Actuators A* 63 (1997) 209–215.

[10] D. Schafer, S. Shoaf, P. Loeppert, Micromachined condenser microphone for hearing aid use, *Proceedings of Solid-State Sensors, Acutators, and Microsystems Workshop*, Hilton Head Island, SC, 1998, pp. 27–30.

[11] A. Torkkeli, O. Rusanen, J. Saarilahti, H. Seppa, H. Sipola, J. Hietanen, Capacitive microphone with low-stress polysilicon backplate, *Sensors and Actuators A* 85 (2000) 116–123.

[12] P. Rombach, M. Mullenborn, U. Klein, K. Rasmussen, The first low voltage, low noise differential silicon microphone, technology development and measurement results, *Sensors and Actuators A* 95 (2002) 196–201.

[13] P.V. Loeppert, S.B. Lee, SiSonic™—the first commercialized MEMS microphone, *Proceedings of Solid-State Sensors, Actuators, and Microsystems Workshop,* Hilton Head Island, SC, 2006, pp. 27–30.

[14] Y. Iguchi, M. Goto, M. Iwaki, A. Ando, K. Tanioka, T. Tajima, F. Takeshi, S. Matsunaga, Y. Yasuno, Silicon microphone with wide frequency range and high linearity, *Sensors and Actuators A* 135 (2) (2007) 420–425.

[15] F.V. Hunt, *Electroacoustics: the Analysis of Transduction and its Historical Background*, Acoustical Society of America, New York, 1954.

[16] D.T. Martin, K. Kadirvel, J. Liu, R.M. Fox, M. Sheplak, T. Nishida, Surface and bulk micromachined dual back-plate condenser microphone, *Proceedings of the 18th IEEE International Conference on Microelectromechanical Systems* (*MEMS'05*), Miami, FL, January 2005, pp. 319–322.

[17] J. Liu, D.T. Martin, K. Kadirvel, T. Nishida, L.N. Cattafesta, M. Sheplak, B.P. Mann, Nonlinear system identification of a MEMS dual-backplate capacitive microphone by harmonic balance method, *Proceedings of ASME International Mechanical Engineering Congress and Exposition* (*IMECE'05*), Orlando, FL, November 2005, paper no. IMECE2005-82880.

[18] R.P. van Kampen, M.J. Vellekoop, P.M. Sarro, R.F. Wolffenbuttel, Application of electrostatic feedback to critical damping of an integrated silicon capacitive accelerometer, *Sensors and Actuators A* 43 (1994) 100–106.

[19] S.D. Senturia, *Microsystems Design*, Kluwer Academic Publishers, Boston, MA, 2001.
[20] M. Rossi, *Acoustics and Electroacoustics*, Artech House, Norwood, MA, 1988.
[21] S. Timoshenko, S.W. Krieger, *Theory of Plates and Shells*, McGraw-Hill, New York, 1959.
[22] M. Sheplak, J. Dugundji, Large deflections of clamped circular plates under tension and transitions to membrane behavior, *Journal of Applied Mechanics* 65 (1) (1998) 107–115.
[23] D.T. Blackstock, *Fundamentals of Physical Acoustics*, Wiley, New York, 2000.
[24] Z. Skvor, On the acoustical resistance due to viscous losses in the air gap of electrostatic transducers, *Acustica* 19 (1967) 295–299.
[25] D. Homentcovschi, R.N. Miles, Modeling of viscous damping of perforated planar microstructures applications in acoustics, *Journal of Acoustical Society of America* 116 (2004) 2939–2947.
[26] J. Liu, D.T. Martin, K. Kadirvel, T. Nishida, M. Sheplak, B.P. Mann, Nonlinear identification of a capacitive dual-backplate MEMS microphone, *Proceedings of ASME International Design Engineering Technical Conferences* (*IDETC'05*), Long Beach, CA, September 2005, paper no. DETC2005-84591.
[27] A.H. Nayfeh, D.T. Mook, *Nonlinear Oscillations*, Wiley, New York, 1979.
[28] User Manual: Laser Doppler Vibrometer, Polytec PI, Inc., Auburn, MA, USA.
[29] S.C. Chapra, R.P. Canale, *Numerical Methods for Engineers: with Software and Programming Applications*, McGraw-Hill, New York, 2002.
[30] H.W. Coleman, W.G. Steele, *Experimentation and Uncertainty Analysis for Engineers*, Wiley, New York, 1999.
[31] MEMS Advanced Design Short Course Notes, Sandia National Laboratories, Albuquerque, NM, July 23–25, 2002.
[32] W.N. Sharpe, K.M. Jackson, K.J. Hemker, Z. Xie, Effect of specimen size on Young's modulus and fracture strength of polysilicon, *Journal of Microelectromechanical Systems* 10 (2001) 317–326.
[33] International Organization for Standardization, *Guide to the Expression of Uncertainty in Measurement*, ISO, Geneva, 1993, ISBN 92-67-10188-9.
[34] S. Chowdhury, M. Ahmadi, W.C. Miller, Nonlinear effects in MEMS capacitive microphone design, *Proceedings of the 2003 International Conference on MEMS, NANO and Smart Systems* (*ICMENS'03*), Baniff, Alberta, Canada, July 2003, pp. 297–302.